

# Distant Horizontal Ground Observation: Atmospheric Perturbation Simulation and Image Restoration

M. Lemaitre  
DGA/DET/CEP/ASC/GIP/SRO  
94114 Arcueil Cedex, France  
Magali.Lemaitre@etca.fr

O. Laligant  
Le2i Laboratory, University of Burgundy  
71200 Le Creusot, France  
o.laligant@iutlecreusot.u-bourgogne.fr

F. Mériaudeau  
Le2i Laboratory, University of Burgundy  
71200 Le Creusot, France  
f.meriaudeau@iutlecreusot.u-bourgogne.fr

J. Blanc-Talon  
DGA/D4S/MRIS  
00303 Armées, France  
Jacques.Blanc-Talon@etca.fr

## Abstract

*Atmospheric perturbation is certainly the most important degradation when observing a scene horizontally at a distance of several kilometers. Because such images with short time exposure are expensive to obtain, they have to be simulated. The goal of this paper is to adapt simulation and restoration of images perturbed by atmospheric turbulence to the case of horizontal ground observation at a large distance and with a short exposure time.*

*The first part of this paper is dedicated to the simulation process. First physical characteristics of atmospheric turbulence are exposed. Then the simulation algorithm is detailed and is adapted to both the anisoplanatic and isoplanatic cases. Simulations have been made with different ratios  $D/r_0$  corresponding to different turbulence intensity values at two wavelengths: one in the visible domain and another in the near infrared domain. Moreover the generation of image sequences where the temporal evolution of the atmospheric turbulence for a fixed scene (i.e. without camera motion) is taken into account, is studied. Indeed the temporal atmospheric turbulence evolution is a key element to be considered when recovering the original scene is desired. The method to obtain such a sequence is explained and an extract of simulated sequence is given and commented.*

*In the second part of this paper, four different classical restoration methods have been tested on these image sets, which can only be used with single frames and need also some knowledge about the original image. To cope with this problem a more recent method has been tried: it is especially adapted to image sequences degraded by atmospheric turbulence. Comparisons have*

*been made between the different obtained results. To conclude some perspectives are given.*

## Introduction

Atmospheric turbulence severely limits the resolution of ground-based cameras and telescopes. Astronomers have been the first confronted with this problem in the context of vertical line of sight. Techniques have been implemented to increase the resolution: interferometry, deconvolution, adaptive optics...

Because of the temporal evolution of the turbulence, these techniques require the use of cameras working at very short exposure times in order to “freeze” the turbulence. Up to now this technology is expensive and is not affordable on a current basis for horizontal observation at a distance of several kilometers. So images have to be simulated, which is done in the first section.

The first part of this section is dedicated to the simulation of single frames perturbed by atmospheric turbulence at two different wavelengths. In the second one, image sequence simulation is explained and an example is given. The second section deals with the comparison of different restoration methods and their suitability to such images.

## A. Simulation

The algorithm of Nicolas Roddier [1] was used to generate the expected perturbations. To simulate an image perturbed by atmospheric turbulence, one has to generate a random turbulent wavefront which leads to an image corresponding to the transfer function of both the atmosphere and the camera at a given instant. Then one

just has to make a convolution with the scene image to obtain a turbulence degraded image. Image sequences have also been simulated taking into account the temporal evolution of atmospheric turbulence.

### A.1. Physical characteristics

**A.1.1. Wavefront perturbation.** A plane wavefront is perturbed by the atmosphere. Only phase calculation is considered during the simulation of a perturbed wavefront. Indeed the effects of amplitude variations correspond to weak scintillation and are negligible compared to those of phase variations. Physically dephasing creates effects of blurring, local shifting, warping...

Only the case of horizontal propagation in the lowest atmosphere layer is treated. The structure constant  $C_N^2$  is approximately the same along the propagation path. The parameter  $C_N^2$  is the amplitude of the refractive index fluctuations spectrum and it gives the influence of turbulence on optical propagation. It depends on local atmospheric conditions (temperature, pressure, humidity rate, wind speed, sun rate...), on the altitude, and on the day/night cycle. Near the ground it also depends on the ground itself (desert, continental, sea...). In this paper, a continental ground is considered.  $C_N^2$  values range between  $10^{-17} \text{ m}^{-2/3}$  (weak turbulence) and  $10^{-12} \text{ m}^{-2/3}$  (strong turbulence). The typical measured mean value of  $C_N^2$  is about  $10^{-14} \text{ m}^{-2/3}$  [2].

**A.1.2. Ratio  $D/r_0$ .** In the literature atmospheric turbulence is often observed for a  $D/r_0$  about 3.  $D$  is the pupil diameter and  $r_0$  is the Fried parameter [3], i.e. the diameter of the wave coherence area or the maximal diameter of the pupil surface for which the perturbed wave can be considered as plane.

Here are the values used in this paper. In the visible domain we took  $\lambda = 550 \text{ nm}$ ,  $L = 10 \text{ km}$  and  $C_N^2 = 10^{-15} \text{ m}^{-2/3}$ . According to Fried formula in the case of horizontal propagation [4] we have:

$$r_0 = 3.02 \times \left( \frac{2\pi}{\lambda} \right)^{-6/5} L^{-3/5} (C_N^2)^{-3/5},$$

so  $r_0 \approx 4 \text{ cm}$ . A pupil which diameter is about 12 cm would be well-adapted to observe atmospheric turbulence at this wavelength.

In the near infrared domain (3-5  $\mu\text{m}$ ) we took  $\lambda = 4 \mu\text{m}$ ,  $L = 5 \text{ km}$  and  $C_N^2 = 5.10^{-14} \text{ m}^{-2/3}$ , which gives  $r_0 \approx 6.4 \text{ cm}$ . A pupil which diameter is about 20 cm would be well-adapted to observe atmospheric turbulence with these parameters.

For comparison images with different values of  $D/r_0$  have been simulated which is equivalent to make vary the pupil size while fixing all other parameters.

### A.2. Generation of a turbulent wavefront

To generate a wavefront degraded by atmospheric turbulence the algorithm of N. Roddier [1] begins by the decomposition of this wavefront phase onto the Zernike polynomials basis which is often used in astronomy.

**A.2.1. Zernike polynomials.** The first orders correspond to the classical aberrations of an optical system. Zernike polynomials are defined on a disk which radius is unity, in each point  $\mathbf{r}$  with polar coordinates  $(r, \theta)$ , by the following expressions:

$$\left. \begin{aligned} Z_{j,\text{pair}} &= \sqrt{n+1} R_n^m(r) \sqrt{2} \cos(m\theta) \\ Z_{j,\text{impair}} &= \sqrt{n+1} R_n^m(r) \sqrt{2} \sin(m\theta) \end{aligned} \right\} m \neq 0$$

$$Z_j = \sqrt{n+1} R_n^0(r) \quad m = 0$$

$$\text{with: } R_n^m(r) = \sum_{s=0}^{(n-m)/2} \frac{(-1)^s (n-s)!}{s! [(n+m)/2-s]! [(n-m)/2-s]!} r^{n-2s}.$$

Each Zernike polynomial is the product of an angular function by a radial polynomial  $R_n^m(r)$ . One can either use the order number  $j$  or the index  $m$  and  $n$  named respectively azimuthal frequency and radial order. These are entire numbers satisfying the relations:  $m \leq n$  and  $n - |m|$  even. The order number  $j$  of a given polynomial is linked to  $m$  and  $n$  by the following relations:

$$n = \lfloor (\sqrt{8j-7} - 1) / 2 \rfloor,$$

$$m = 1 + 2 \lfloor (j - 1 - \lfloor n(n+1)/2 \rfloor) / 2 \rfloor \quad n \text{ odd},$$

$$m = 2 \lfloor (j - \lfloor n(n+1)/2 \rfloor) / 2 \rfloor \quad n \text{ even},$$

with  $\lfloor \cdot \rfloor =$  Entire Part.

On Figure 1 the aspect of the first simulated Zernike polynomials from  $Z_1$  ( $n=0, m=0$ ) to  $Z_{21}$  ( $n=5, m=5$ ) are shown. Some polynomials are compared with classical optical aberrations. The polynomial  $Z_4$  ( $n=2, m=0$ ) is the one which has the most influence on the image degradation. It takes the aspect of defocusing. The "piston" mode corresponds to the polynomial  $Z_1$  which is constant.

**A.2.2. Turbulent wavefront phase.** The phase of a turbulent wavefront on a pupil, which radius is  $R$ , is given by:

$$\varphi(r, \theta) = \sum_j a_j Z_j \left( \frac{r}{R}, \theta \right).$$

The coefficients of the decomposition are the projections of the phase  $\varphi$  on the basis functions:

$$a_j = \frac{1}{S} \int P(\mathbf{r}) \varphi(\mathbf{r}) Z_j(r/R) dr,$$

where  $P(\mathbf{r})$  is the transmission function of the pupil which radius is  $R$  and which surface is  $S$ . The simulation consists of randomly generating a set of coefficients  $\{a_j\}$  in such a way that the obtained phase respects

Kolmogorov statistics (it is the case with atmospheric turbulence).

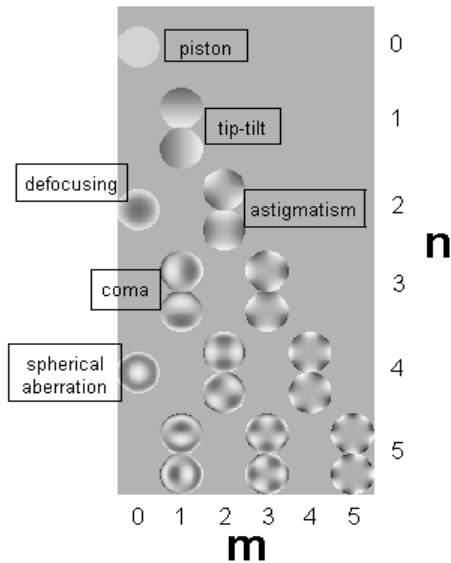


**Figure 1. Comparison of the first Zernike polynomials with optical aberrations.**

*Remark:* To verify that the simulated phase written  $\varphi(\mathbf{r})$  follows Kolmogorov statistics one calculates the phase structure function which is the phase fluctuation variance between two points distant of  $\rho$  and defined by:

$$D_\varphi(\rho) = \langle |\varphi(\mathbf{r} + \rho) - \varphi(\mathbf{r})|^2 \rangle,$$

and it is compared to the theoretical structure function of a phase which follows Kolmogorov statistics (Fig. 2), and whose expression is [3]:

$$D_\varphi(\rho) = 6.88 (\rho / r_0)^{5/3},$$

where  $\rho = |\rho|$ .

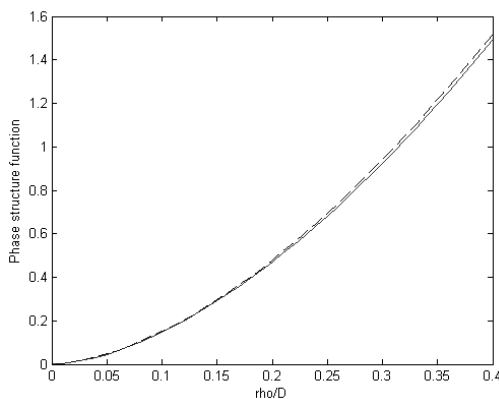


**Figure 2. Comparison between simulated and Kolmogorov phase structure functions near the pupil center (D = pupil diameter): [- - -] theory, [—] simulation.**

Zernike coefficients of an atmospheric wavefront can be considered as random Gaussian variables with zero mean and a certain variance [5]. Nevertheless a wavefront cannot be directly simulated by only generating these Zernike coefficients: Zernike polynomials are not statistically independent, there exists a non-zero covariance between some of the Zernike coefficients [1]. Noll derived an expression of this covariance [5] which, in the Fourier domain, is a Zernike matrix representation of the Kolmogorov phase spectrum.

To obtain statistically independent random variables, one has to carry out the calculation in an orthonormal basis where vectors are completely decorrelated: we choose the basis formed by the Karhunen-Loève polynomials. Although they don't have an analytical expression, they can be decomposed onto the Zernike basis like any wavefront which is simply done by diagonalization of the covariance matrix whose expression is given by Noll [5]. Coefficients can then be generated in this new basis by independent random drawings. Zernike coefficients are obtained by going back to the original basis, and thus respect the Kolmogorov model.

The simulated turbulent phase can be written as a decomposition on the Zernike polynomials basis:

$$\varphi(\mathbf{r}) = \sum_{j=2}^J a_j Z_j(\mathbf{r}),$$

where the pupil dimension is implicitly normalized compared with its radius. In this decomposition the "piston" mode which corresponds to the mean phase, is excluded. The sum begins then from the order  $j = 2$ . In practice this sum is limited to a finite number  $J-1$  of Zernike polynomials. In the rest of this paper, a parameter  $J = 135$  was used. To respect the Shannon criteria, a pupil of 64 pixels diameter was used, enrolled in a square of side 64 pixels.

Once the turbulent wavefront is computed, one has just to convolve it to the scene image to yield the related atmospheric perturbed image.

### A.3. Anisoplanatism or isoplanatism?

#### A.3.1. What are anisoplanatism and isoplanatism?

Atmospheric turbulence perturbations on optical beams vary according to these beams propagation direction. Consequently turbulence effects compensation methods (*a posteriori* restoration methods and adaptive optics methods) are limited to a reduced field angle named *isoplanatic domain*. This limitation is due to *anisoplanatism*, i.e. the perturbation depends on the position in the observed object field since the beams descended from different points in the field pass through different layers of the atmosphere [6] (Fig. 3). The two beams suffer from different perturbations: it is anisoplanatism. The hatched zone corresponds to the

atmosphere area where the two beams are degraded in the same way: it is the isoplanatic domain. It is very small compared to the total propagation path.

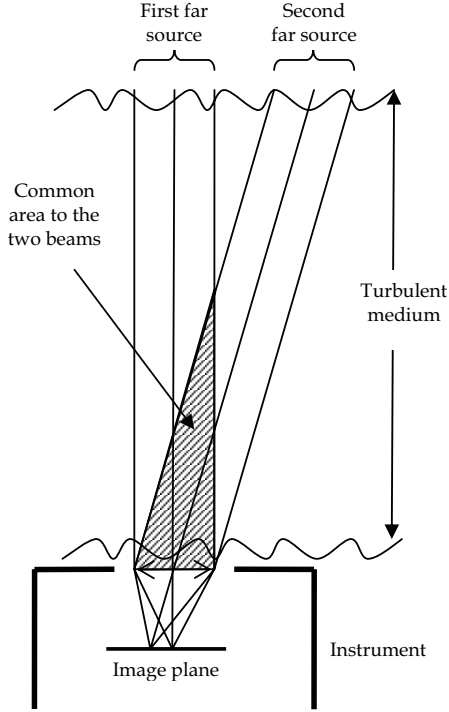


**Figure 3. Origin of atmospheric isoplanatism and anisoplanatism.**

**A.3.2. Case of horizontal propagation.** In the particular case of a horizontal propagation along a path of length  $L$  in a turbulent medium, the structure constant de  $C_N^2$  is almost the same, and according to Fried we have [4]:

$$r_0 = 3.02 \times \left( \frac{2\pi}{\lambda} \right)^{-6/5} L^{-3/5} (C_N^2)^{-3/5},$$

$$\theta_0 = 0.95 \times \left( \frac{2\pi}{\lambda} \right)^{-6/5} L^{-8/5} (C_N^2)^{-3/5},$$

where  $r_0$  is the Fried parameter and  $\theta_0$  is the maximal isoplanatic angle [in rd]. We can also consider that  $\theta_0$  is the minimal angle from which we are in the case of anisoplanatism. So we have:

$$r_0 = 3.18 L \theta_0,$$

with the scheme on Figure 4 [7].

*Pixel resolution and isoplanatic angle:* We are in the case of distant observation (i.e. the distance  $L$  between the scene and the acquisition system represents several kilometres, from 5 to 10 km according to the considered wavelength). For a camera of  $1024 \times 1024$  pixels and a

scene of  $200 \text{ m} \times 200 \text{ m}$  at a distance of 10 km, a pixel side represents about 20 cm of the real scene.

Let us note  $\alpha$  the pixel resolution. Numerically we obtain:  $\alpha \approx 20 \text{ } \mu\text{rd}$ . With Fried formula [4] and the same values as in paragraph 1.3., we have:

- in the visible domain:  $\theta_0 \approx 0.51 \text{ } \mu\text{rd}$ ,

- in the infrared domain:  $\theta_0 \approx 4.02 \text{ } \mu\text{rd}$ .

In both cases the pixel resolution  $\alpha$  is widely larger than the isoplanatic angle  $\theta_0$ : we are obviously in the case of **anisoplanatism**.

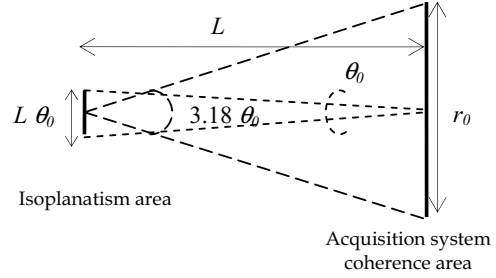


**Figure 4. Link between  $r_0$  and  $\theta_0$ .**

#### A.4. Simulated images examples

In this section short exposure degradation simulation results in both visible and infrared domains will be compared. Simulations have been carried out in total anisoplanatism and also in total isoplanatism. These two following original images have been used (Fig. 5):

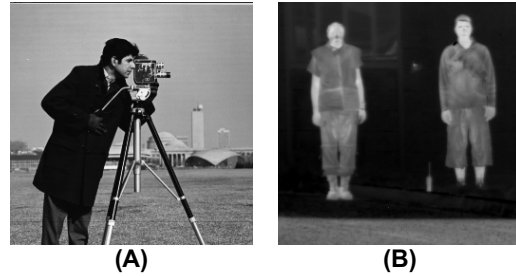


**Figure 5. Original images in both the visible (A) and the infrared (B) domains (256 x 256 pixels).**

**A.4.1. Cameraman in total anisoplanatism.** In the case of total anisoplanatism, each pixel is degraded by a different random wavefront. From a classical image in the visible domain, spatially and temporally decorrelated degradations have been simulated with different values for  $D/r_0$ .

On Figure 6, for a ratio  $D/r_0 = 3$  we can observe a very important degradation and the obtained image looks like an astronomic one when observing a star without adaptive optics or a posteriori restoration. For  $D/r_0 = 1$

we can observe a very granular aspect on the image while foreseeing details on the background. For a ratio  $D/r_0 = 0.1$  the granularity is much fainter and details are clearer. And for  $D/r_0 = 0.01$  the granularity disappeared and gave way to a slight blurring.

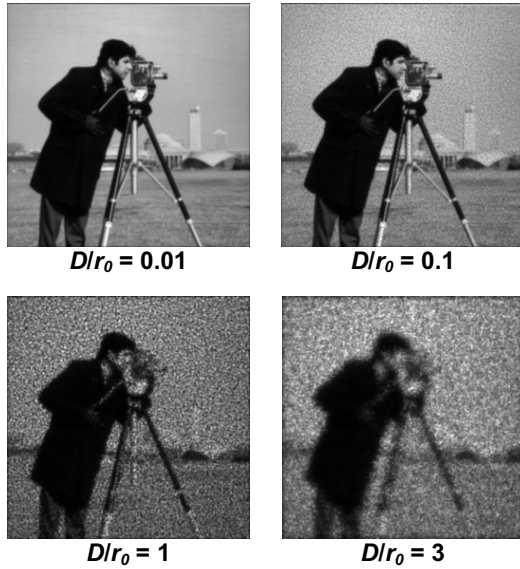


**Figure 6. Random degradations examples in total anisoplanatism with increasing perturbation intensity, in the visible domain.**

**A.4.2. Cameraman in total isoplanatism.** In the case of total isoplanatism, all pixels are degraded by the same random wavefront. From the same original image, for comparison, degradations in total isoplanatism have been simulated with different ratios  $D/r_0$ .

We can observe on Figure 7 that images contain a slight global shifting (for  $D/r_0 = 3$ ) and a blurring which becomes more important as the ratio  $D/r_0$  increases.

**A.4.3. Infrared images in total anisoplanatism.** As in the visible domain, spatially and temporally decorrelated degradations due to atmospheric turbulence have been simulated on an original infrared image with different ratios  $D/r_0$ .

As in the visible case, we can observe (Fig. 8) a very strong degradation for  $D/r_0 = 3$ . This infrared image has a dark and uniform background which permits us to observe the similarity between this image and an astronomical one. The bottom does not seem really degraded while the two men are particularly degraded. For  $D/r_0 = 1$  we can also observe a strong granularity and details seem to be more difficult to identify in the infrared domain than in the visible domain. For a ratio  $D/r_0 = 0.1$  there remains a slight granularity and details in the background appear. And for a ratio  $D/r_0 = 0.01$  the

granular aspect disappeared and gave way to a slight blurring.

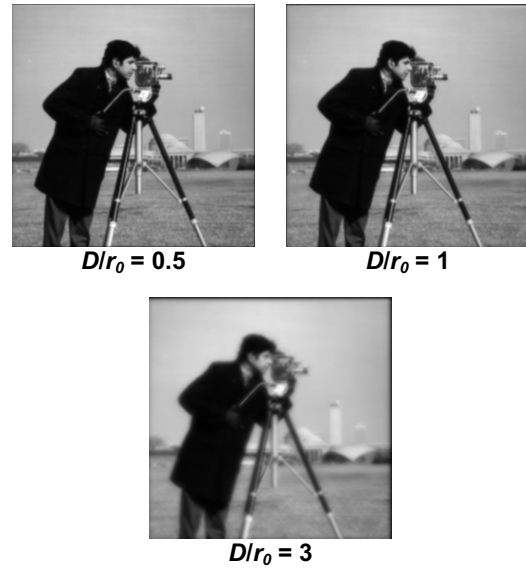


**Figure 7. Random degradations examples in total isoplanatism with increasing perturbation intensity, in the visible domain.**

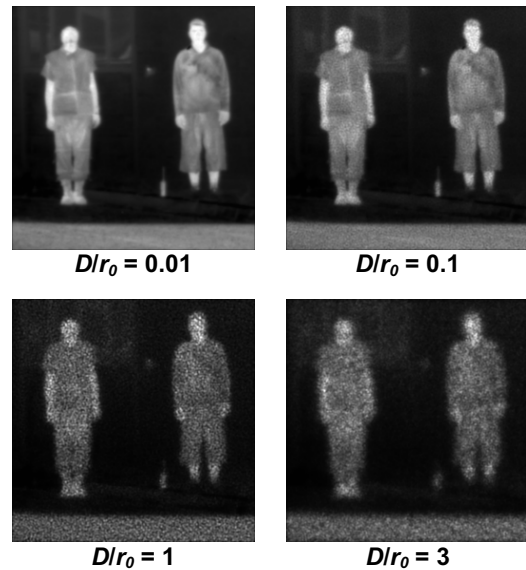


**Figure 8. Random degradations examples in total anisoplanatism with increasing perturbation intensity, in the infrared domain.**

**A.4.4. Conclusion.** Due to the intrinsic definition of infrared images (less contrast and less details), there will be less degradation in the infrared domain. However we

can observe the same kind of perturbation in the visible domain and on the observed objects in the infrared domain (especially a granular aspect for anisoplanatism).

A possible amelioration of the algorithm could be for *local isoplanatism* (i.e. the case between total anisoplanatism and total isoplanatism) to replace the *global* shifting by a *local* one (real situation) which would create local deformations in different directions. This situation would better fit the case where the pixel resolution is close to the isoplanatic angle.

### A.5. Temporal evolution of atmospheric perturbation

In this section we are interested in the simulation of temporal turbulence evolution. The exposure time is considered to be less than 5 ms to make short exposure images. It is chosen small enough to “freeze” the turbulence. To have a long exposure image, it is enough to take the average image of a temporally correlated short exposure images set.

**A.5.1. Temporal evolution of the random Zernike coefficients  $a_j$ .** With the same method as in [7], short exposure image sequences have been simulated taking into account temporal fluctuations of atmospheric turbulence. The principle is to filter a set of temporally independent random coefficients  $a_j$ , and to obtain another set whose power spectral density obeys to the following equation [8]:

$$w_j(\nu) = \frac{1}{V} \int_{-\infty}^{+\infty} \left| \tilde{M}_j\left(\frac{\nu}{V}, f_y\right) \right|^2 W_\phi\left(\frac{\nu}{V}, f_y\right) df_y,$$

where  $\nu$  is the temporal frequency,  $f = (f_x, f_y)$  is the spatial frequency,  $V$  is the wind speed oriented along the  $x$  axis,  $w_j(\nu)$  is the temporal power spectral density of coefficient  $a_j$  at the order  $j$ ,  $W_\phi$  represents the phase spatial power spectrum, and for a Kolmogorov turbulence it is given by:

$$W_\phi(f) = 0.023 r_0^{-5/3} f^{-11/3},$$

and finally  $\tilde{M}_j(f)$  is the Fourier transform of the Zernike polynomial  $Z_j$  and its modulus is [8]:

$$\left| \tilde{M}_j(f) \right| = \sqrt{n+1} \frac{2|J_{n+1}(\pi D f)|}{\pi D f} \begin{cases} \sqrt{2}|\cos(n\theta)| & j \text{ even and } m \neq 0, \\ \sqrt{2}|\sin(n\theta)| & j \text{ odd and } m \neq 0, \\ 1 & m=0, \end{cases}$$

where  $J_l(x)$  is the Bessel function of the first kind at the order  $l$ .

Here is an example of temporal simulation of atmospheric turbulence with the following characteristics:

- acquisition frequency:  $f = 200$  fps
- exposure time: 5 ms
- wind speed:  $V = 6$  m/s (about 22 km/h)
- propagation path length:  $L = 10$  km
- Fried parameter:  $r_0 = 4$  cm

- pupil diameter:  $D = 12$  cm
- wavelength:  $\lambda = 550$  nm.

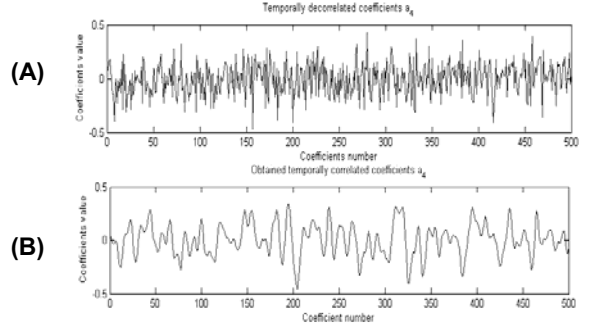


**Figure 9. Samples of 500 temporally uncorrelated (A) and correlated (B) random Zernike coefficients related to polynomial  $Z_4$ .**

On Figure 9 (A) the obtained signal looks like a white noise. Random Zernike coefficients  $a_j$  have been generated independently each other by the method of N. Roddier [1], so they are completely temporally decorrelated. When looking at Figure 9 (B), a clear temporal correlation appears between the random coefficients  $a_j$ . Their evolution is slower, then visually more representative of atmospheric turbulence.

### A.5.2. Simulation example.

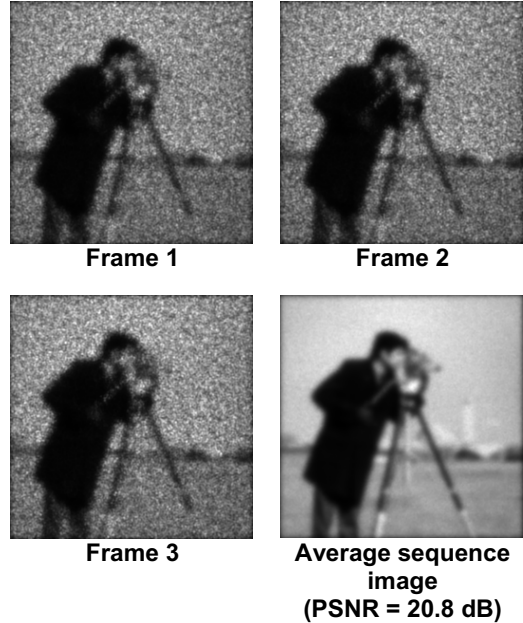


**Figure 10. Extract of a 100 frames sequence in total anisoplanatism with a ratio  $D/r_0 = 3$ , and the average image.**

On Figure 10, even if each frame of the sequence seems much degraded we can see that the average image is clearly less perturbed. This is due to the fact that random coefficients follow a gaussian law in the Karhunen-Loève basis. Some of them are then cancelled during the averaging. Moreover the average image is a long exposure one: the perturbation does not look like granularity but rather like a strong blurring. Some details appear like the tower in the background.

### A.6. Conclusion on simulation

In this first part single frames and then image sequences perturbed by atmospheric turbulence have been simulated. We are especially interested in the case of total anisoplanatism (cf. § A.3.2). That is why we only treat this case in the restoration part.

## B. Restoration

### B.1. Tested methods

Four classical methods processing only single frames were tested on our images (the inverse filter, the Wiener filter, the Tikhonov regularization and the Laplacian regularization). The degradation was approximated by one point spread function.

We also tested a recent method processing a whole image sequence: the “Windowed-Wiener” method [9]. Its principle is to detect a local space-varying point spread function (PSF) describing the atmospheric turbulence. The PSF is found by using a Wiener filter acting on windowed regions-of-interest of a reference image and each image frame of the sequence. The reference image is the average of the sequence and is updated after each deconvolution pass of the complete sequence. The process is repeated until the difference between the two last average images is minimized.

### B.2. Results in the visible domain

The perturbed short exposure image we tried to restore with the four classical methods is shown on Figure 6 with  $D/r_0 = 3$ . We also tried the “Windowed-Wiener” method on the simulated sequence given in example in paragraph A.5.2.

These results (Fig. 11) clearly show the inefficiency of the four classical methods to the case we are dealing with. The inverse filter is particularly unsuited due to its great sensibility to noise. The Tikhonov regularization gives the best PSNR for the classical methods but the edges are more visible with the Wiener filter in spite of a poorly restored background.

In spite of the presence of a subsisting blurring, the result with the Windowed-Wiener method is visually much better than those obtained with classical methods,

which is confirmed by a higher PSNR. The strength of this method results from the fact that the average image is used, giving a low frequency approximation of the true image. Secondly the local Wiener filter enables to better recover edges and details. For instance one can distinguish columns of the buildings in the background.

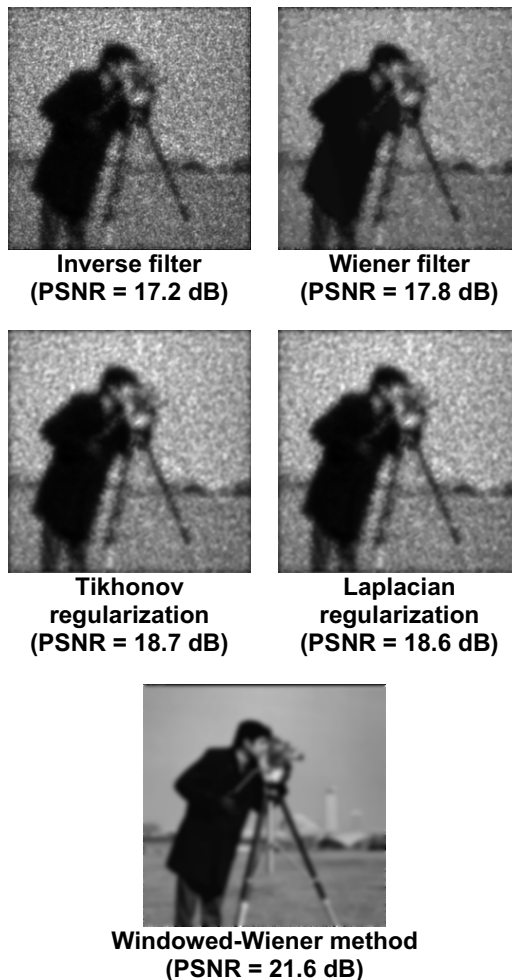


**Figure 11. Some restoration results in the visible domain.**

### B3. Results in the infrared domain

We first tried the four classical methods on the image on Figure 8 with  $D/r_0 = 3$ . Then in the same way as in the visible domain, an infrared sequence has been simulated in total anisoplanatism with the same ratio  $D/r_0 = 3$ , and the Windowed-Wiener method was tested on this sequence.

Results are shown in Figure 12. Once again the four classical methods are shown to be unsuited to our

images. However the Laplacian regularization gives the best PSNR. Globally the PSNR in the infrared case is higher than in the visible case. This is due to the fact that infrared images contain fewer details. The average image gives a better PSNR than the classical methods and the Windowed-Wiener method improves significantly the obtained result.

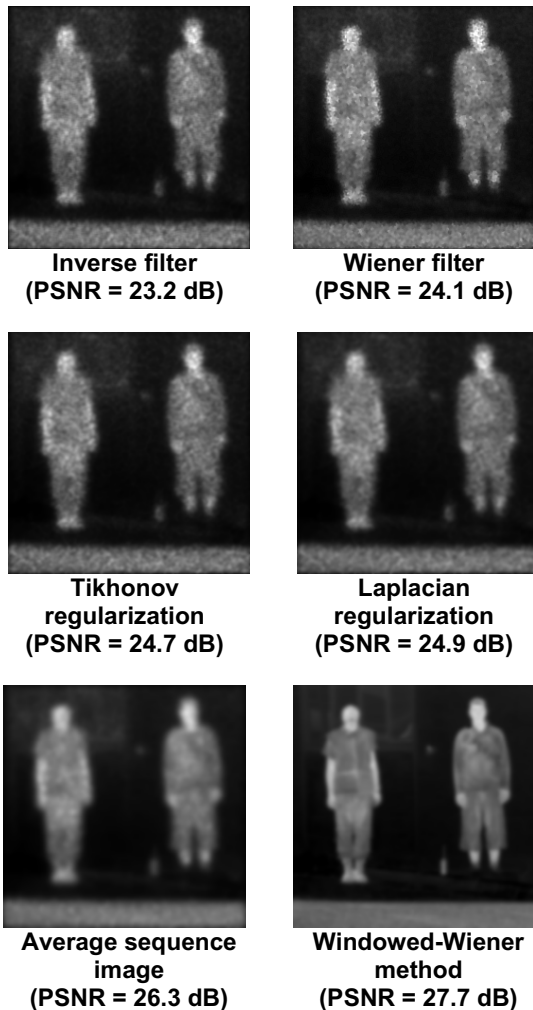


**Figure 12. Some restoration results in the infrared domain.**

## Conclusion

This paper was dedicated to the simulation and the restoration of atmospheric perturbation in the case of horizontal ground observation at a large distance. First physical characteristics of atmospheric turbulence were talking about. Then the simulation algorithm was explained and adapted to both the anisoplanatic and

isoplanatic cases. Simulations have been made with different ratios  $D/r_0$  at two wavelengths. Global remarks have been made for these two wavelengths, and differences have been noted for the infrared case where less degradation appears. Moreover image sequences have been simulated where we took into account the temporal evolution of the atmospheric turbulence. The method to obtain such a sequence was explained and an example was given. We noted that the simulation algorithm could be improved by introducing spatial correlation for the case of local isoplanatism.

In the second part of this paper, different classical restoration methods have been tested on these image sets: the inverse filter, the Tikhonov regularization, the Laplacian regularization, and the Wiener filter. These four methods give naturally bad results. A more recent method called “Windowed-Wiener” has been tried too and is especially adapted to image sequences perturbed by atmospheric turbulence as shown by the obtained results. One could include in this algorithm a readjusting step for sequences with camera or scene motion, which would give a better reference image.

## Bibliography

- [1] N. Roddier, Atmospheric wavefront simulation using Zernike polynomials, *Optical Engineering*, 29 (10): 1174-1180, 1990.
- [2] D. L. Hutt, Modeling and measurements of atmospheric optical turbulence over land, *Optical Engineering*, 38 (8): 1288-1295, August 1999.
- [3] D. L. Fried, Optical Resolution Through a Randomly Inhomogeneous Medium for Very Long and Very Short Exposures, *Journal of the Optical Society of America*, 56 (10): 1372-1379, October 1966.
- [4] D. L. Fried, Anisoplanatism in adaptive optics, *Journal of the Optical Society of America*, 72 (1): 52-61, January 1982.
- [5] R. J. Noll, Zernike polynomials and atmospheric turbulence, *Journal of the Optical Society of America*, 66 (3): 207-211, 1976.
- [6] F. Chassat, Calcul du domaine d’isoplanétisme d’un système d’optique adaptative fonctionnant à travers la turbulence atmosphérique, *J. Optics*, 20 (1): 13-23, Paris, 1989.
- [7] C. Bondeau-Zimmer, *Etude d’images perturbées par la turbulence atmosphérique : Simulation et Restauration*, PhD Thesis, University of Burgundy, Dijon, 1999.
- [8] J. M. Conan, G. Rousset, P. Y. Madec, Wavefront temporal spectra in high resolution imaging through turbulence, *Journal of the Optical Society of America A*, 12 : 1559-1570, 1995.
- [9] D. Fraser, A. Lambert, *Information Retrieval From a Position-Varying Point Spread Function*, ACIVS Conference, Brussels, Belgium, 2004.